J. Fluid Mech. (2011), *vol.* 672, *pp.* 219–244.
doi:10.1017/S0022112010005926

Peristaltic pumping of rigid objects in an elastic tube

D. TAKAGI[1] AND N. J. BALMFORTH[2,3]†

[1]Institute of Theoretical Geophysics, Department of Applied Mathematics and Theoretical Physics, University of Cambridge, Wilberforce Road, Cambridge CB3 0WA, UK

[2]Department of Mathematics, University of British Columbia, 1984 Mathematics Road, Vancouver, V6T 1Z2, Canada

[3]Department of Earth and Ocean Science, University of British Columbia, 6339 Stores Road, Vancouver, V6T 1Z4, Canada

(Received 14 April 2010; revised 3 November 2010; accepted 10 November 2010; first published online 24 February 2011)

A mathematical model is developed for long peristaltic waves propelling a suspended rigid object down a fluid-filled axisymmetric tube. The fluid flow is described using lubrication theory and the deformation of the tube using linear elasticity. The object is taken to be either an infinitely long rod of constant radius or a parabolic-shaped lozenge of finite length. The system is driven by a radial force imposed on the tube wall that translates at constant speed down the tube axis and with a form chosen to generate a periodic wave train or a solitary wave. These waves exert a traction on the enclosed object, forcing it into motion. Periodic waves drive the infinite rod at a speed that attains a maximum at a moderate forcing amplitude and approaches approximately one quarter of the wave speed in the large-amplitude limit. The finite lozenge can be entrained and driven at the same speed as a solitary wave or periodic wave train if the forcing is sufficiently strong. For weaker forcing, the lozenge is either left behind the solitary wave or interacts repeatedly with the waves in the periodic train to generate stuttering forward progress. The threshold forcing amplitude for entrainment increases weakly with the radial span of the enclosed object, but strongly with the axial length, with entrainment becoming impossible if the object is too long.

Key words: lubrication theory, peristaltic pumping, solitary waves

1. Introduction

Biological systems often transport solid objects suspended in a fluid lubricant by the mechanism of peristalsis. For example, the peristaltic pumping of sperm cells is fundamental to reproduction (Fauci & Dillon 2006), and the digestive system requires the transport of many kinds of contents including rigid medical pills. Consequently, in addition to providing a novel problem of fluid–structure interaction, the dynamics of the peristaltic pumping of a solid object has important biological applications.

The current article follows on from a companion paper (Takagi & Balmforth 2011; henceforth referred to as Part 1) in which we present an elastohydrodynamic lubrication theory for the peristaltic pumping of axisymmetric ducts filled purely with fluid. Here, we generalize that theory to include a movable, slender, rigid object

† Email address for correspondence: njb@math.ubc.ca

suspended within the fluid-filled duct. A key feature of the model is that we treat the wall of the duct as an elastic solid with its own dynamics and drive peristaltic motion directly by prescribing active stresses on the wall. This distances our model from many previous ones which specify the displacement of the wall and therefore ignore any elastic tube mechanics (e.g. Shapiro, Jaffrin & Weiberg 1969). The model is therefore arguably more relevant to the biological applications, especially when the peristaltic motion acts to propel a suspended solid object.

Previous work on the peristaltic pumping of fluid suspensions has often focused on relatively small objects, motivated by bacterial transport. When the suspended objects are sufficiently small, they may be regarded as passive tracers, and so the degree of transport can be judged by following fluid streamlines (Shapiro *et al.* 1969). Although slightly larger particles may still not appreciably affect the overall flow field, motion relative to the fluid can also occur, demanding a separate study of the particle paths (Hung & Brown 1976; Srivastava & Srivastava 1989; Jiménez-Lozano, Sen & Dunn 2009). In contrast, we consider more extreme situations in which the object suspended in the fluid is sufficiently large to modify significantly the flow field.

Previous studies along these lines include those of Lighthill (1968) and Fitz-Gerald (1969), who considered the dynamics of red blood cells squeezing through narrow capillaries. Lighthill allowed elastic deformation of both the capillary wall and blood cell, treating in detail the narrow lubrication layers sandwiched between the cell and tightly surrounding wall. Lighthill's model is different from, but complementary to, our current model because we consider relatively slender objects and long peristaltic waves, applying lubrication theory to the whole arrangement. Other potential biological applications include the transport of the embryo in the uterus (Eytan & Elad 1999), gallstones in the bile duct and kidney stones in the ureter.

Although our combination of lubrication theory with linear elasticity allows us to extract detailed results from a relatively simple model, the assumptions implicit in these choices have limitations in regard to real biological applications. For example, linear elasticity may provide a poor representation of the mechanics of biological ducts (Fung 1971; Carew & Pedley 1997), and by taking the object to be rigid we rule out the possibility that it may change shape or size as it is pumped forward (as for Lighthill's red blood cells). Moreover, we assume that the object remains along the centreline of the tube, leading to an axisymmetric configuration. Such centred states may be unstable or not exist if the object or tube is not axisymmetric, and the object might then drift off-axis and rotate, inducing a more complicated flow state. Nevertheless, the simplicity of the model allows us to offer a relatively complete picture of how the dynamics depends on physical parameters such as the forcing strength and the size of the object to be pumped, and to access various limits of the physical problem analytically. We thereby complement some recent computational studies of a less idealized nature (Bertuzzi *et al.* 1983; Fauci 1992; Connington *et al.* 2009).

We formulate the problem mathematically in § 2. We then investigate how different rigid objects are pumped by peristaltic waves of either periodic or solitary form: in § 3, we consider how an infinitely long rod is driven forward by a periodic wavetrain. Though unable to displace such an object, we also consider the effect of solitary waves on an infinite rod in § 4. In contrast, in § 5, we show that a solitary wave of sufficient forcing amplitude is able to entrain a finite object and drive it forward at the wave speed. Finally, in § 6, a finite object pumped by a periodic wavetrain is shown to either move together with the waves or experience time-periodic motion with mean speed less than the wave speed.

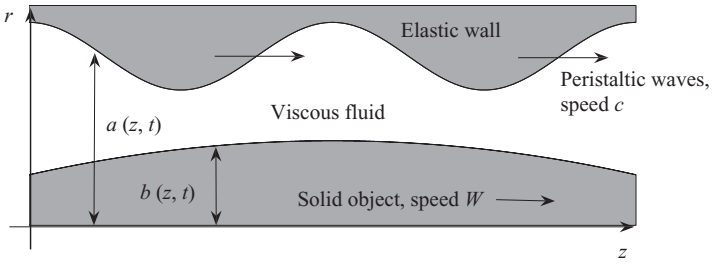

FIGURE 1. A sketch of the geometry, showing the (axisymmetrical) elastic tube with the forced peristaltic waves and the central rigid object thereby propelled forward.

2. Mathematical formulation

Consider a rigid body of revolution with radius $\hat{b}(\hat{z},\hat{t})$, immersed in an incompressible fluid of density ρ and dynamic viscosity μ, and all enclosed within a flexible tube of radius $\hat{a}(\hat{z},\hat{t})$, as sketched in figure 1. The arrangement is axisymmetric and the contents of the tube are propelled along in the axial direction by a radially directed, moving body force applied on the tube wall with a form $\hat{F}(\hat{z}-c\hat{t})=\hat{\eta}f[(\hat{z}-c\hat{t})/L]$, where c denotes the propulsion speed, $\hat{\eta}$ and L represent the characteristic strength and axial scale of the forcing, and f is a dimensionless function describing the spatial structure. We assume that the back reaction on the tube due to the propulsion of the contents is countered by an external support, so that the tube itself does not translate bodily in the axial direction, but is fixed in the laboratory frame. The rod has a central position $\hat{Z}(\hat{t})$ and axial speed $\hat{W}(\hat{t})$.

2.1. *Dimensional equations*

Invoking the lubrication approximation, the velocity field, $(\hat{u},\hat{w})$, and pressure, $\hat{p}$, of the induced fluid flow satisfy

$$\frac{1}{\hat{r}}\frac{\partial}{\partial\hat{r}}(\hat{r}\hat{u})+\frac{\partial\hat{w}}{\partial\hat{z}}=0,\quad \frac{\partial\hat{p}}{\partial\hat{r}}=0,\quad \frac{\partial\hat{p}}{\partial\hat{z}}=\frac{1}{\hat{r}}\frac{\partial}{\partial\hat{r}}\left(\hat{r}\mu\frac{\partial\hat{w}}{\partial\hat{r}}\right). \tag{2.1}$$

The boundary conditions include force balance and no slip between the fluid and the tube wall or object. Because the arrangement is slender, as the wall squeezes the fluid, the main resistance is provided by the normal pressure force and fluid tractions remain much smaller (as in many other lubrication problems with flexible surfaces; see, for example, Skotheim & Mahadevan 2005). Consequently, the tube deforms mainly radially, and

$$\frac{\partial\hat{a}}{\partial\hat{t}}=\hat{u}\quad\text{and}\quad\hat{w}=0\quad\text{on}\quad\hat{r}=\hat{a}. \tag{2.2}$$

The propelled object, on the other hand, moves rigidly at speed $\hat{W}$:

$$\frac{\partial\hat{b}}{\partial\hat{t}}+\hat{W}\frac{\partial\hat{b}}{\partial\hat{z}}=0\quad\text{and}\quad\hat{w}=\hat{W}\quad\text{on}\quad\hat{r}=\hat{b}. \tag{2.3}$$

If the propelled object has a finite length, and therefore only occupies part of the domain, we replace conditions (2.3) with the condition that $\partial\hat{w}/\partial\hat{r}=0$ along the tube axis, $\hat{r}=0$.

For the axial boundary conditions, we consider either periodic domains or the infinite axial problem. For the latter, we demand that all disturbances to the flow and deformations of the tube decay as $\hat{z}\to\pm\infty$ (precluding any pressure drop from one end of the tube to the other).

We model the cylindrical tube as a linearly elastic material such that the force balance on the elastic tube is

$$\hat{p}(\hat{a}, \hat{z}, \hat{t}) - p_0 = \hat{D}(\hat{a} - R) + F, \tag{2.4}$$

where p_0 is the ambient pressure, R is the equilibrium tube radius attained in its undeformed state, and the parameter $\hat{D}$ measures the stiffness of the tube. Although this model applies strictly when the tube deformations are not large, our theoretical discussion in subsequent sections extends to larger-amplitude limits, where effects of nonlinear elasticity may play an important role. However, the model becomes substantially more convoluted on adding such effects, and we prefer to retain the simplicity of the formulation afforded by (2.4) in order to extract as many explicit results as possible.

In the absence of any other body forces, the traction exerted on the object by the fluid dictates its acceleration (whereas the elastic tube is externally supported so that it cannot translate along its axis). That is,

$$\hat{M}\frac{\mathrm{d}\hat{W}}{\mathrm{d}\hat{t}} = 2\pi \int_{\mathscr{D}} \left[\hat{p}\frac{\partial \hat{b}}{\partial \hat{z}} + \mu \frac{\partial \hat{w}}{\partial \hat{r}} \right]_{\hat{r}=\hat{b}} \hat{b}\, \mathrm{d}\hat{z}, \tag{2.5}$$

where $\hat{M}$ denotes the mass and $\mathscr{D}$ represents either the periodic or infinite axial domain. The first term in square brackets on the right-hand side corresponds to the drag acting on the object due to pressure variations in the fluid and the second term corresponds to the tangential stresses arising from fluid viscosity. We ignore any pressure load on the front and back of the object by taking the object radius to taper gradually to zero at the ends (rendering $\partial\hat{b}/\partial\hat{z}$ finite, and assuming that the lubrication approximation remains valid there) or by considering an infinitely long rod. We retain the object's inertia in (2.5), but use the Stokes approximation for the fluid for two reasons. First, the approximation is justified if the fluid gap is relatively narrow, $\hat{a} - \hat{b} \ll \hat{b}$, or if the object is relatively dense (bearing in mind that the fluid shear stresses scale with gap thickness rather than object radius in the thin-gap limit). Second, later, when we solve the equations numerically, it proves expedient (if not essential) for the particular numerical scheme to retain the differential character of (2.5), taking an inertial parameter related to $\hat{M}$ (denoted by M below) to be small.

2.2. *Dimensionless formulation*

We now remove the dimensions from the equations by defining the new variables

$$\left.\begin{aligned} &z = \frac{\hat{z} - c\hat{t}}{L}, \quad r = \frac{\hat{r}}{R}, \quad t = \frac{c\hat{t}}{L}, \quad Z(t) = \frac{\hat{Z}}{L}, \quad W(t) = \frac{\hat{W}}{c}, \quad [a(z,t), b(z,t)] = \frac{1}{R}(\hat{a}, \hat{b}), \\ &u(r,z,t) = \frac{R\hat{u}}{cL}, \quad w(r,z,t) = \frac{\hat{w}}{c} - 1, \quad p(r,z,t) = \frac{(\hat{p} - p_0)R^2}{\mu c L}, \end{aligned}\right\} \tag{2.6}$$

and dimensionless parameters

$$D = \frac{\hat{D}R^2}{\mu c}, \quad \eta = \frac{\hat{\eta}R}{\mu c}, \quad M = \frac{c\hat{M}}{2\pi\mu L^2}. \tag{2.7}$$

Note that these relations effect a transformation of the fluid equations into the frame of reference of the peristaltic waves, although the object's position and speed remain relative to the laboratory frame. The fluid equations then imply that the pressure is

independent of radius, $p = p(z, t)$, and

$$\frac{1}{r}\frac{\partial}{\partial r}\left(r\frac{\partial w}{\partial z}\right) = \frac{\partial p}{\partial z}, \qquad \frac{1}{r}\frac{\partial}{\partial r}(ru) + \frac{\partial w}{\partial z} = 0. \tag{2.8}$$

Integrating the first of these and imposing the no-slip boundary conditions leads to

$$w = -\frac{1}{4}\frac{\partial p}{\partial z}(a^2 - r^2) + \left[W + \frac{1}{4}\frac{\partial p}{\partial z}(a^2 - b^2)\right]\frac{\log(a/r)}{\log(a/b)} - 1. \tag{2.9}$$

The integral form of mass conservation can then be determined to be

$$\frac{\partial}{\partial t}(a^2 - b^2) + \frac{\partial Q}{\partial z} = 0, \tag{2.10}$$

where

$$Q = 2\int_b^a wr\,\mathrm{d}r = b^2 - a^2 - \frac{1}{8}\frac{\partial p}{\partial z}\left[a^4 - b^4 - \frac{(a^2 - b^2)^2}{\log(a/b)}\right] + \frac{W(a^2 - b^2)}{2\log(a/b)} - b^2 W. \tag{2.11}$$

The dimensionless version of the force law (2.4) for the elastic tube is

$$p = D(a - 1) + \eta f(z), \tag{2.12}$$

and the dimensionless equation of motion (2.5) for the propelled object reduces to

$$M\frac{\mathrm{d}W}{\mathrm{d}t} = -\int_{\mathscr{D}}\left[W + \frac{1}{4}(a^2 - b^2)\frac{\partial p}{\partial z}\right]\frac{\mathrm{d}z}{\log(a/b)}, \tag{2.13}$$

since there is no difference in $b^2 p$ across the domain of interest. This holds both in the periodic and infinite domains, the former because of periodicity and the latter because the radius of a finite object is assumed to taper gradually to zero at the ends, $b \to 0$, with finite slope.

2.3. *Energetics*

From (2.8)–(2.13) we may derive a statement of energy balance:

$$-2\pi\int_{\mathscr{D}} ap\,u(a, z, t)\,\mathrm{d}z \equiv -2\pi\int_{\mathscr{D}} ap\left(\frac{\partial a}{\partial t} - \frac{\partial a}{\partial z}\right)\mathrm{d}z = \varepsilon + \frac{\mathrm{d}}{\mathrm{d}t}(\pi M W^2), \tag{2.14}$$

where the energy dissipation rate is

$$\varepsilon = 2\pi\int_{\mathscr{D}}\int_b^a \left(\frac{\partial w}{\partial r}\right)^2 r\,\mathrm{d}r\,\mathrm{d}z, \tag{2.15}$$

$$\equiv 2\pi\int_{\mathscr{D}}\left\{\frac{1}{16}\left(\frac{\partial p}{\partial z}\right)^2\left[a^4 - b^4 - \frac{(a^2 - b^2)^2}{\log(a/b)}\right] - \frac{(a^2 - b^2)W}{4\log(a/b)}\frac{\partial p}{\partial z} - \frac{W^2}{\log(a/b)}\right\}\mathrm{d}z. \tag{2.16}$$

Note that, for steady waves, we may discard the time derivatives and directly balance the power input due to the forcing with the viscous dissipation rate:

$$2\pi\eta\int_{\mathscr{D}} af\frac{\mathrm{d}a}{\mathrm{d}z}\,\mathrm{d}z \equiv -\pi\eta\int_{\mathscr{D}} a^2\frac{\mathrm{d}f}{\mathrm{d}z}\,\mathrm{d}z = \varepsilon, \tag{2.17}$$

a result we make use of later.

3. Periodic waves driving an infinite rod

We study how periodic peristaltic waves drive an infinite rod by taking b and W to be constant and seeking steady solutions, $a = a(z)$. In this situation, the quantity

$$q = Q - b^2 + 1 = 1 - a^2 - \frac{1}{8}\frac{\mathrm{d}p}{\mathrm{d}z}\left[a^4 - b^4 - \frac{(a^2-b^2)^2}{\log(a/b)}\right] + \frac{W(a^2-b^2)}{2\log(a/b)} - b^2 W \qquad (3.1)$$

is constant and is proportional to the time-averaged flux of fluid in the laboratory frame. In the limit as $b \to 0$, q in (3.1) reduces to the corresponding flux explored exhaustively in Part 1 for peristaltic transport without the rod. Note that this limit is seemingly singular in the sense that one can reduce (3.1) to the objectless version of the problem without difficulty, yet the two problems have quite different boundary conditions on $w(r, z, t)$ along $r = 0$ (according to the no-slip boundary condition, the axial velocity is uniform at $r = 0$ with an infinitely thin object, but when there is no object whatsoever, $w(0, z, t)$ varies with z). In fact, it is clear from (2.9) that the velocity field has a boundary layer around the tube axis for $r = O(b)$, wherein the flow predicted from the objectless problem becomes corrected such that no-slip is satisfied. However, this structure does not impact the dynamics of the tube. The equation of motion for the rigid object in this limit follows from multiplying (2.13) by $\log(1/B)$, where $B = \mathrm{Max}(b)$, and then taking $B \to 0$ with $M\log(1/B) \to 0$ (and taking the object's mass to scale with its maximum radius). This last operation leads to the problem considered in § 6.2.

Rearranging (3.1) and introducing the force law for the tube wall (2.12) leads to the differential eigenvalue problem,

$$\frac{1}{8}\left[a^4 - b^4 - \frac{(a^2-b^2)^2}{\log(a/b)}\right]\left[D\frac{\mathrm{d}a}{\mathrm{d}z} + \eta f'(z)\right] = 1 - q - a^2 - b^2 W + \frac{W(a^2-b^2)}{2\log(a/b)}. \qquad (3.2)$$

The eigenvalues q and W are determined by imposing the constraints

$$\langle a^2 \rangle = 1 \qquad (3.3)$$

and

$$\left\langle \left[W + \frac{1}{4}\frac{\mathrm{d}p}{\mathrm{d}z}(a^2 - b^2)\right]\frac{1}{\log(a/b)} \right\rangle = 0, \qquad (3.4)$$

where the angular brackets denote the average over a spatial period, $\langle\cdot\rangle = \int_0^{2\pi}(\cdot)\mathrm{d}z/2\pi$. Condition (3.3) follows from mass conservation (given our choice of radial length scale) and (3.4) follows from the equation of motion of the propelled object (2.13). As in Part 1, for purposes of illustration we adopt the sinusoidal forcing

$$f(z) = \sin z. \qquad (3.5)$$

Below, we present solutions to the eigenvalue problem formulated above, fixing the stiffness parameter at $D = 1$ but varying η and b. As illustrated in Part 1, the limits of small and large stiffness offer analytical inroads into the problem. However, there are no significant qualitative differences in the dynamics when this parameter is varied, so for the current work we leave it fixed. More relevant are variations in the forcing amplitude and object radius.

3.1. *Low forcing amplitude*

In the limit of small η, a regular perturbation expansion of the equations can be performed using the asymptotic sequences, $a = 1 + \eta a_1 + O(\eta^2)$, $q = \eta^2 q_2 + O(\eta^4)$ and

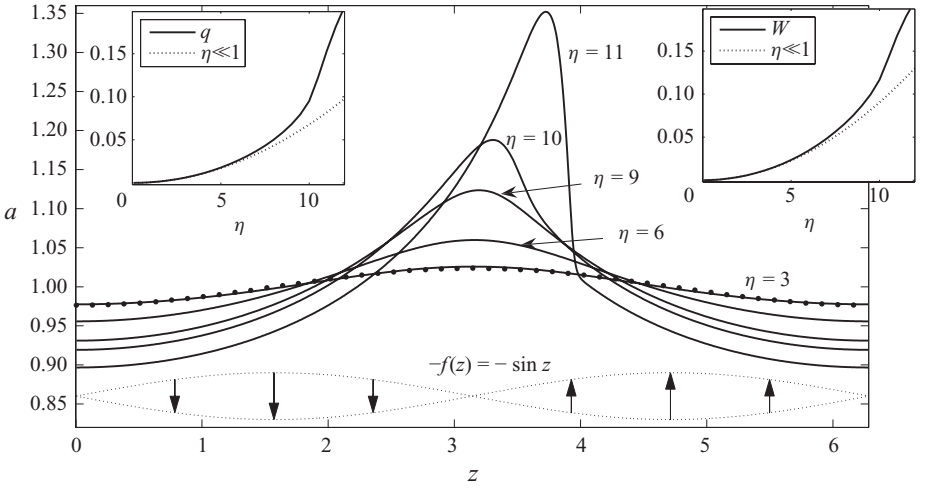

FIGURE 2. In the main panel, wave profiles for $b = 1/2$, $D = 1$, and differing forcing amplitudes (as indicated) are shown alongside the dots representing the low-amplitude profile predicted by (3.7) with $\eta = 3$. The arrows show the magnitude and direction of the applied radial force (as given by $-f(z) = -\sin z$). The two insets respectively show the fluid transport q and the object speed W plotted against the forcing amplitude; the dashed lines show the low-amplitude predictions given by (3.9) and (3.8).

$W = \eta^2 W_2 + O(\eta^4)$. To order η, (3.2) reduces to

$$kD\frac{\mathrm{d}a_1}{\mathrm{d}z} + 16a_1 = -k\cos z, \qquad k = 1 - b^4 + \frac{(1-b^2)^2}{\log b}. \tag{3.6}$$

Hence,

$$a = 1 - \eta\frac{16k\cos z + k^2 D\sin z}{(kD)^2 + 16^2} + O(\eta^2). \tag{3.7}$$

The solution (3.7) can be substituted into the integral constraint (3.4) to obtain

$$W = \frac{2k}{(kD)^2 + 16^2}\left(2 + \frac{1-b^2}{\log b}\right)\eta^2 + O(\eta^4). \tag{3.8}$$

and taking the spatial average of (3.1) furnishes

$$q = \frac{2k}{(kD)^2 + 16^2}\left(2 + \frac{1-b^2}{\log b}\right)(1-b^2)\eta^2 + O(\eta^4). \tag{3.9}$$

3.2. *Numerical results for higher forcing amplitude*

Numerical solutions of the eigenvalue problem with increasing forcing amplitude are shown in figure 2 (computed using MATLAB's BVP4C, with relative and absolute tolerances for errors of 10^{-3} and 10^{-6}, respectively). The deformations in tube radius resemble those found for the fluid problem in Part 1, with a pronounced peak developing and shifting towards the maximum of the applied outward radial force, $z = 3\pi/2$, as η increases. A relatively large-amplitude solution is shown in figure 3 and features a narrow blister surrounding $z = 3\pi/2$, adjoining an occlusion of the tube (the example shown has an inner rod of radius $b = 1/2$, which a approaches outside the blister).

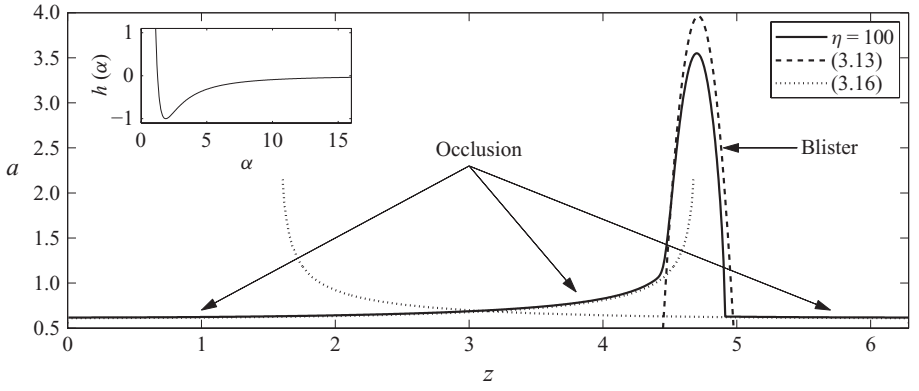

FIGURE 3. A large-amplitude solution with $\eta = 100$, $D = 1$ and $b = 1/2$. The dotted lines show the occluded solutions from (3.16) and the dashed line displays the peak solution (3.13). The inset shows the function $h(\alpha)$ defined in (3.16).

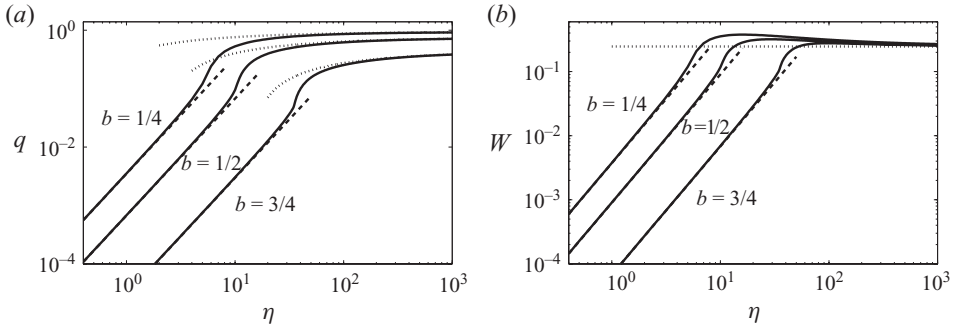

FIGURE 4. (*a*) Transport q and (*b*) object speed W against the forcing amplitude η for $D = 1$ and three different rod radii, b (as indicated). The dotted lines show the large-amplitude limiting solutions in (3.15) and the dashed lines show the low-amplitude results (3.9) and (3.8).

More details of the variation of the eigenvalues q and W, with η and b, are shown in figure 4. Note that the object attains a maximal speed at moderate η because, at higher forcing amplitudes, the tube develops the narrow occlusion which heightens the viscous resistance. This impedes the propulsion of the rod, thereby reducing W, and the object speed eventually approaches a constant, b-independent value, $W \sim 0.247$. Simultaneously, the flux approaches $1 - b^2$, implying a near-complete transport of the fluid within the gap between the rod and the tube. We rationalize these observations in § 3.3 by constructing an asymptotic solution for $\eta \gg 1$.

Figure 5 plots the energy dissipation rate against forcing amplitude, which increases as $32\pi^2 k\eta^2/(k^2+16^2)$ for $D = 1$ at low forcing amplitude (and follows from substituting the low-amplitude solution (3.7) into (2.17)). Once η is order one, however, ε flattens out, and then increases again at high amplitude with the slower dependence $\eta^{1/2}$. The increasing dissipation at high amplitude contrasts sharply with results derived in Part 1, where ε approaches a constant for $\eta \gg 1$, with the occlusion of the tube countering the heightened forcing over the constricted regions that dominate the dissipation. With the central rod, however, the tube cannot become arbitrarily constricted, allowing the increased forcing to outpace the reduction in tube radius within the occlusion, thereby raising the dissipation. Figure 5 also plots a measure of pumping efficacy, W/ε, the axial speed of the object per unit input of power.

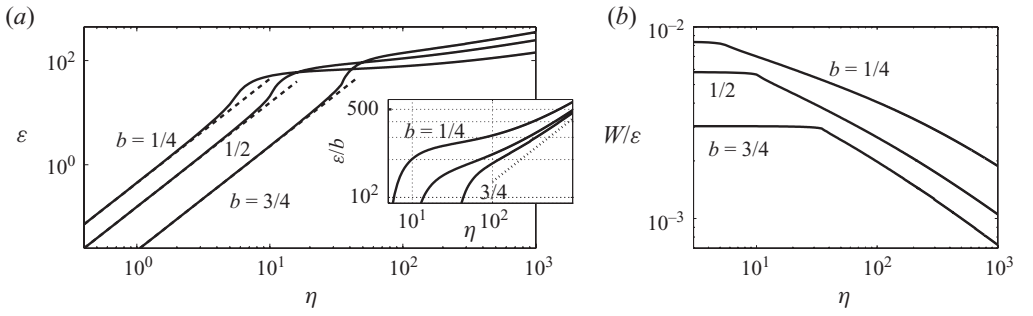

FIGURE 5. (*a*) Dissipation rate ε against forcing amplitude η for $D = 1$ and three different rod radii, b (as indicated). The dashed lines show the low-amplitude result $\varepsilon \sim 32\pi^2 k\eta^2/(k^2+16^2)$ for $D = 1$. The inset redraws the data as ε/b; the dotted line shows the expected large-amplitude solution in (3.20). In (*b*), the same data are used to plot the efficacy W/ε.

This quantity is independent of η and equal to $[1 + (1 - b^2)/\log(b^2)]/8\pi^2$ at low forcing amplitudes, but then decreases like $\eta^{-1/2}$ in the large-amplitude limit. We conclude that pumping of an infinitely long rod is most effective at the lowest forcing amplitudes and the smallest rod radii.

3.3. *Large-amplitude solutions*

The large-amplitude solution can be built by matched asymptotic expansions, piecing together solutions for the blister and occlusion across slender intervening boundary layers. The details of the boundary layers have little consequence (cf. Part 1), so we focus only on the leading-order structure of the blister and occlusion.

In the narrow blister, we rescale the axial coordinate and tube radius to resolve the relatively sharp features of the large-amplitude solution. In (3.2), the dominant terms are

$$\frac{1}{8}a^4\left[D\frac{\mathrm{d}a}{\mathrm{d}z} + \eta f'(z)\right] \equiv \frac{1}{8}a^4\frac{\mathrm{d}p}{\mathrm{d}z} \sim 0, \tag{3.10}$$

indicating that the blister is maintained by a combination of the forcing, tube stiffness and a constant fluid pressure. This leads us to set

$$z - \tfrac{3}{2}\pi = \eta^{-2/5}\zeta, \qquad a = \eta^{1/5}A(\zeta), \qquad p = -\eta + O(\eta^{1/5}), \tag{3.11}$$

after Taylor expanding the forcing function about $z = 3\pi/2$, and in view of the fact that most of the fluid is contained in the blister, which implies

$$1 = \langle a^2\rangle \to \frac{1}{2\pi}\int_{-\delta}^{\delta} A^2(\zeta)\,\mathrm{d}\zeta + b^2, \tag{3.12}$$

where $\zeta = \pm\delta$ denote the edges of the blister. Those edges arise where $A(\zeta \to \pm\delta) = 0$, which is needed to match the blister to the much lower amplitude solution outside that region where $a \to b$. Thus, solving (3.10) and reverting to the original variables, we find

$$a \sim a_{max} - \frac{\eta}{2D}\left(\frac{3\pi}{2} - z\right)^2, \tag{3.13}$$

where the peak radius

$$a_{max} = \left[\frac{15^2\pi^2(1-b^2)^2\eta}{2^3 D}\right]^{1/5}. \tag{3.14}$$

This solution is compared with the $\eta = 100$ numerical result in figure 3.

Over the occluded region, $a \to b$, and the largest terms on the right-hand side of (3.2) balance the forcing on the left. This reflects how the flow between the occluded tube and the rod generates a lubrication pressure that counters the forcing, and the detailed balance of terms implies the characteristic scalings,

$$a \sim b + \eta^{-1/2}\alpha, \qquad W \sim W_\infty \qquad \text{and} \qquad q \sim 1 - b^2 - \eta^{-1/2} b \hat{q}, \tag{3.15}$$

where α, W_∞ and $\hat{q}$ are order unity, and the additional factor of b is included in the correction to q to remove the dependence of W_∞ and $\hat{q}$ on the rod radius, as shown below.

Substitution of (3.15) into (3.1) gives, to leading order, an implicit equation for α:

$$\cos z = h(\alpha) \equiv \frac{6}{\alpha^3}\,[\hat{q} - \alpha\,(2 - W_\infty)]. \tag{3.16}$$

As illustrated by the inset of figure 3, the function h has the asymptotic limits, $h \to \infty$ as $\alpha \to 0$ and $h \to 0$ as $\alpha \to \infty$, together with a local minimum of $h(\alpha_+) = -3\hat{q}/\alpha_+^3 < 0$ at $\alpha_+ = 3\hat{q}/(4 - 2W_\infty) > 0$ (the rod speed does not exceed the wave speed $W_\infty < 1$, and the correction $\hat{q}$ is positive because the fluid flux does not reverse). Thus, the solution is multivalued, and we must suitably select the correct branch. As illustrated in figure 3, the occluded large-η eigenfunction tracks the lowest branch of solutions for $z < \pi$ and $3\pi/2 < z$, but the larger one for $\pi < z < 3\pi/2$ (aside from the insertion of the blister solution in the vicinity of $z = 3\pi/2$). In order that the eigenfunction passes smoothly through $z = \pi$, the two branches of (3.16) must intersect at $z = \pi$, which demands $h(\alpha_+) = -1$ and

$$\hat{q} = \frac{2^{3/2}}{3}\,(2 - W_\infty)^{3/2}\,. \tag{3.17}$$

A second equation relating W_∞ and $\hat{q}$ follows from (3.4). The contributions to this integral are dominated by the occluded region, and by substituting (3.16) into (3.4) and keeping only the leading-order terms of order $\eta^{1/2}$, we obtain

$$\left\langle \frac{2W_\infty}{\alpha} + \alpha \cos z \right\rangle = 0 \tag{3.18}$$

or

$$(4W_\infty - 6)\langle \alpha^{-1} \rangle + (4 - 2W_\infty)^{3/2} \langle \alpha^{-2} \rangle = 0. \tag{3.19}$$

This is an algebraic equation for W_∞, given (3.16), which may be solved using Newton iteration: we adopt a trial value of W_∞, and then evaluate numerically the integrals in (3.19) after dividing the integration range into the three regions, $0 \leqslant z \leqslant \pi$, $\pi < z < 3\pi/2$ and $3\pi/2 < z < 2\pi$, and changing the integration variable from z to α. The subsequent iteration leads to $W_\infty \approx 0.247$, and then $\hat{q} \approx 2.19$ from (3.17), in agreement with solutions plotted in figure 4.

Finally, the dissipation rate (2.17) is dominated by the occluded region and given by

$$\varepsilon \sim -4\pi^2 \eta^{1/2} b \langle \alpha \cos z \rangle = 8\pi^2 b \eta^{1/2} W_\infty \langle \alpha^{-1} \rangle \approx 13.3 b \eta^{1/2}, \tag{3.20}$$

which is compared with the numerical data in the inset of figure 5, and provides the limiting pumping efficacy, $W_\infty/\varepsilon \sim 0.0185 b^{-1} \eta^{-1/2}$.

4. Solitary waves with an infinite rod

In Part 1, we have shown how fluid can be pumped by solitary waves as well as periodic wavetrains. The corresponding problem with a central uniform rod results in $W=0$ because a finite solitary wave cannot drive an infinitely long object. Nevertheless, we provide a brief analysis of this problem because it is a limiting case of the problem with an object of finite length. Moreover, the stationary inner rod can also be thought of as an artificial stent, adding relevance to other practical applications (Cummings *et al.* 2004; Siggers *et al.* 2008).

For steady solitary waves, $a(z,t)\to a(z)$ with $a\to 1$ as $z\to\pm\infty$. Then, from (3.1), and keeping $W\neq 0$ for the moment,

$$q = W\left(\frac{1-b^2}{2\log b^{-1}} - b^2\right). \tag{4.1}$$

The equation of motion (2.13) now reduces to

$$M\frac{\mathrm{d}W}{\mathrm{d}t} + \frac{W}{\log b^{-1}}\int_{\mathscr{D}} \frac{(a^2+b^2)\log(1/b) - 1 + b^2}{(a^2+b^2)\log(a/b) - a^2 + b^2}\,\mathrm{d}z = \tau, \tag{4.2}$$

where

$$\tau = \int_{\mathscr{D}} \frac{2(a^2-1)\,\mathrm{d}z}{(a^2+b^2)\log(a/b) - a^2 + b^2}. \tag{4.3}$$

In addition to the acceleration term, the left-hand side of (4.2) contains the drag incurred by moving the rod at speed W along the tube, and the right-hand side is the traction exerted by the solitary waves. Thus, if the forcing and therefore a^2-1 are appreciable only within a localized section of the tube, and the rod is uniform and of a much longer length, ℓ, we expect $W\sim\tau\ell^{-1}\log b^{-1}$.

For illustration, we adopt the solitary-wave forcing given by

$$f = \mathrm{e}^{-z^2/2}. \tag{4.4}$$

Numerical solutions for steady wave profiles with $q=W=0$ are shown in figure 6. As for the rod-less results presented in Part 1, the tube increasingly deforms as η is raised, developing large-amplitude bow waves running ahead of the forcing for $\eta\gg 1$. The fluid transport associated with the waves can be measured with the quantity (cf. Part 1),

$$\Delta = 2\int_{-\infty}^{\infty}\int_{b}^{a}(w+1)r\,\mathrm{d}r\,\mathrm{d}z \equiv \int_{-\infty}^{\infty}(a^2-1)\,\mathrm{d}z, \tag{4.5}$$

which is plotted against the forcing amplitude in figure 6, along with the traction τ and dissipation rate ε. The quantities Δ, τ, and ε all scale like η^2 in the low-amplitude limit, as found earlier in § 3 for periodic waves. In the large-amplitude limit, the fluid transport and the traction are dominated by the bow wave, meaning that $\Delta\sim\eta^5$ as presented in Part 1 and $\tau\sim\eta^3/\log\eta$ because (4.3) scales like $1/\log\eta$ times η^3, the length of the bow wave. The dissipation rate $\varepsilon\sim\eta^3$ because it is dominated by the occluded region, like in § 3.3 and as outlined in Part 1.

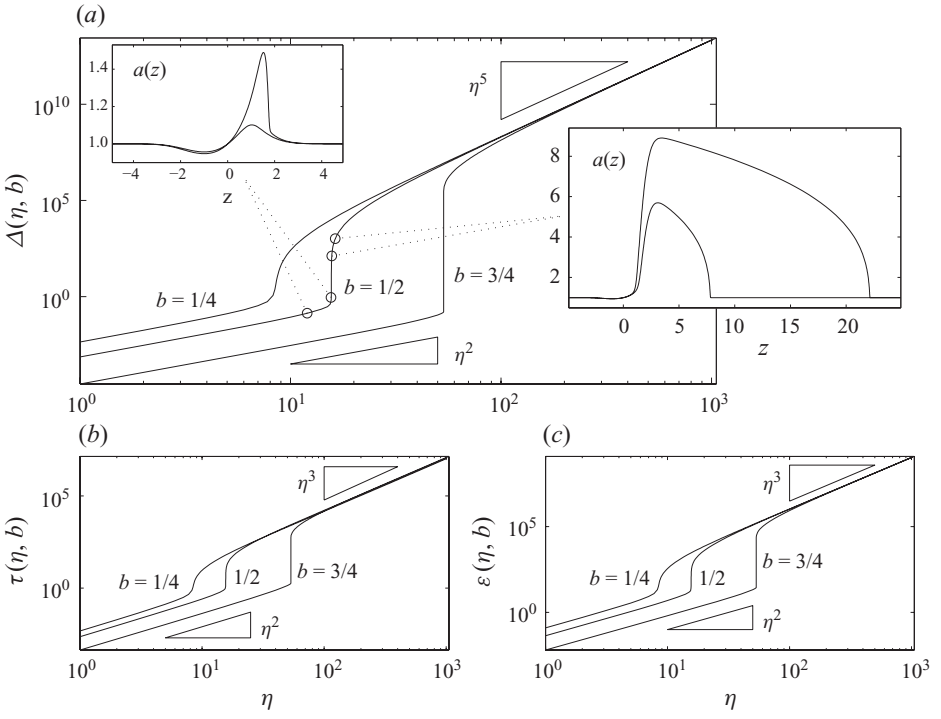

FIGURE 6. Solitary waves travelling along a tube with a central static rigid rod. (*a*) The fluid transport Δ against the forcing amplitude η. The insets show sample wave profiles at the forcing amplitudes indicated. (*b*, *c*) The traction τ on the rod and the dissipation rate ε, respectively.

5. Solitary-wave pumping of a finite object

We now move on to consider a finite object driven by a solitary wave. By way of an example, we adopt the forcing (4.4) and set

$$b = B\ \mathrm{Max}\left(1 - \frac{4(z - Z + t)^2}{\ell^2}, 0\right), \tag{5.1}$$

i.e. our object is a parabolic-shaped lozenge of length ℓ and maximum radius B. Throughout our exploration, we set $M = 0.1$, a value that we verified was sufficiently small to eliminate any significant effect of particle inertia.

5.1. *The initial-value problem and capture*

We first solve the differential equations (2.10)–(2.13) numerically as an initial-value problem. To begin the computation, we take an undeformed fluid-filled tube without any enclosed object and instantaneously turn on the forcing at $t = 0$. The equations are solved by approximating the spatial derivatives with centred finite differences on a uniform grid of 500 points or more (depending on the fine structure in the solution). The resulting ordinary differential equations are then integrated in time using a standard stiff scheme (MATLAB's ODE15s, which has an adaptive time step that is chosen to maintain relative and absolute errors of less than 10^{-3} and 10^{-6}, respectively). The domain (which lies in the frame of the forcing) is truncated to the left and right, where we impose the boundary conditions $a = 1$. The locations of the boundaries are chosen to be sufficiently far from the localized forcing that they have

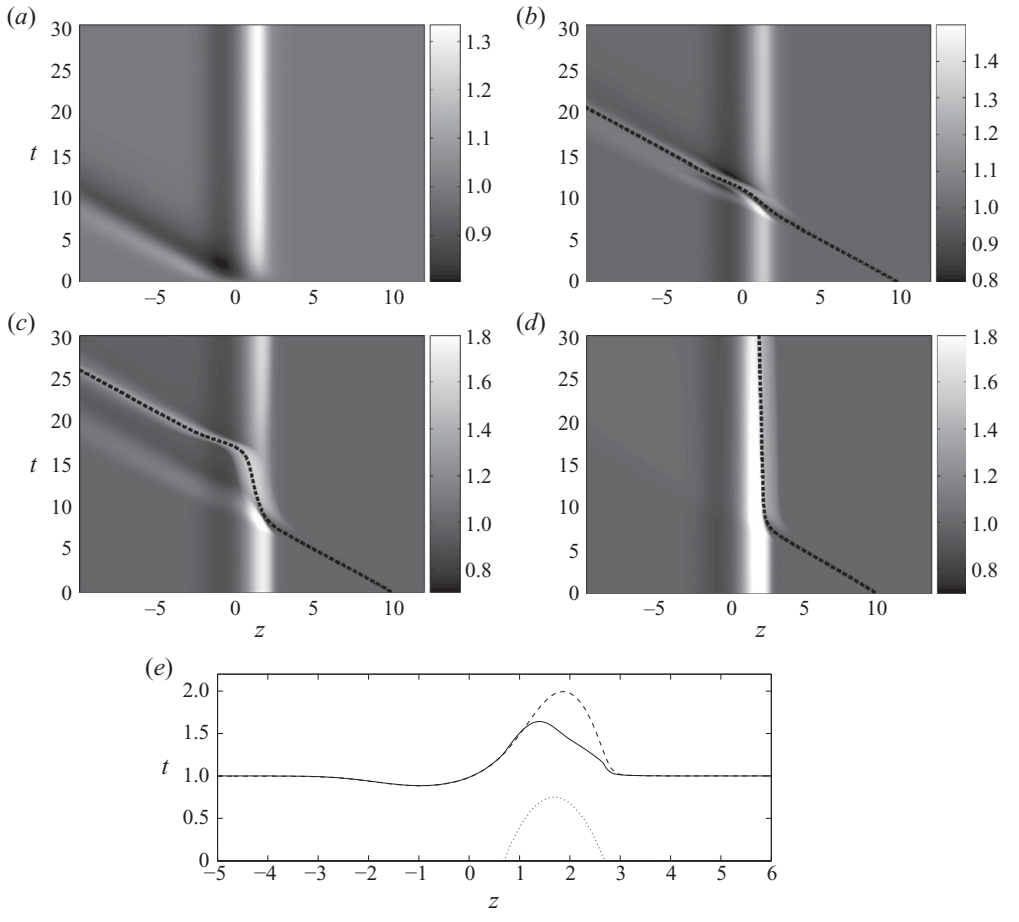

FIGURE 7. Initial-value problems showing the tube radius $a(z, t)$ as a density on the (z, t)-plane. (a) The initial set-up of the problem in which an originally uniform tube is deformed by the switch-on of the forcing at $t = 0$ to generate a solitary peristaltic wave ($\eta = 3.6$). In (b), the computation is restarted with an object centred at $z = Z(0) = 10$ upstream of the solitary wave; the centre of the object, $z = Z(t)$, is shown by the dotted line. The remaining parameter settings are $\ell = 2$, $B = 0.5$, $M = 0.1$ and $D = 1$, and the domain is $[-10, 17]$. (c, d) Similar computations with $\eta = 4.36$ and $\eta = 4.6$, respectively. (e) The initial and final profiles of the computation with $\eta = 4.6$ (the solid line is the final snapshot of $a(z, t)$, the dashed line is $a(z, 0)$, and the dotted line is the final $b(z, t)$).

no significant effect on the peristaltic dynamics. Later, when we consider peristaltic driving by periodic wavetrains, we adopt periodic boundary conditions instead.

The switch-on of the forcing generates a disturbance that settles into a propagating solitary wave. An example is shown in figure 7(a); the disturbance is partly left behind (and propagates to the left in the frame of the forcing), with the remainder developing into the steady wave. Structures of this kind can be computed more directly using the ordinary differential equations satisfied by steadily propagating solutions, as in Part 1.

Once the solution has settled into steady state, we terminate the computation and restart it with the same solitary wave but also including an object further upstream. The solitary wave then propagates into the object, pushing it to the right. With the

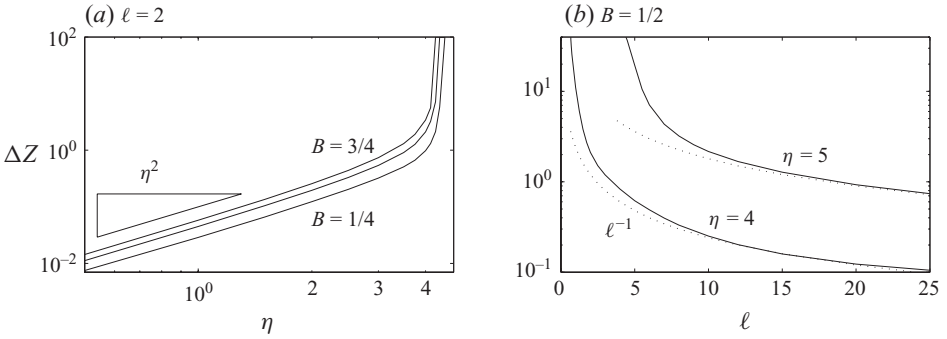

FIGURE 8. Final displacements, $\Delta Z = Z(\infty) - Z(0)$, against ($a$) forcing amplitude η and (b) particle length ℓ. In (a), three particle radii are shown ($B = 1/4$, $1/2$ and $3/4$). In (b), $B = 1/2$ and two forcing amplitudes are shown; the dotted lines show a large-ℓ fit with $\Delta Z \sim \ell^{-1}$.

lower forcing amplitude of $\eta = 3.6$ shown in figure 7(b), the solitary wave is only able to shift the position of the object slightly, which is then left behind. Raising the forcing amplitude to $\eta = 4.36$ strengthens the solitary wave such that it is able to move the object significantly, but still not entrain it. At yet higher forcing amplitude ($\eta = 4.6$), the solitary wave captures the object and the two then propagate together, adjusting into a stable steady arrangement (see figure 7d).

The initial-value computations reveal two important features of the dynamics: first, there is a threshold in the strength of the solitary wave below which the object cannot be captured. As we approach the threshold from below, the total displacement suffered by the particle due to the passage of the wave diverges, as seen in figure 8. Second, above the threshold, the system converges to a steadily propagating wave–particle combination. These latter steady states can again be constructed more directly, as we describe below.

5.2. *Steady particle-entraining waves*

Setting the time derivatives to zero in (2.10) implies that the flux Q in (2.11) is constant in space. Furthermore, since $a \to 1$, $b \to 0$ and $f' \to 0$ as we proceed upstream or downstream, $Q = -1$. The steady arrangements resulting from the capture of the object by the solitary wave also travel at the speed of the forcing, $W = 1$. The position of the object in the wave frame $z = Z$, however, must be adjusted to ensure force balance. Altogether, the equations to be satisfied are therefore

$$\frac{\mathrm{d}p}{\mathrm{d}z} \equiv D\frac{\mathrm{d}a}{\mathrm{d}z} + \eta f'(z) = 8\left[1 - a^2 + \frac{(a^2 - b^2)}{2\log(a/b)}\right]\left[a^4 - b^4 - \frac{(a^2 - b^2)^2}{\log(a/b)}\right]^{-1} \tag{5.2}$$

and

$$\int_{Z-\ell/2}^{Z+\ell/2} \left[1 + \frac{1}{4}\frac{\mathrm{d}p}{\mathrm{d}z}(a^2 - b^2)\right]\frac{\mathrm{d}z}{\log(a/b)} = 0. \tag{5.3}$$

This system amounts to another differential eigenvalue problem, this time with the object position Z playing the role of eigenvalue.

Numerical solutions to the eigenvalue problem for $B = 3/4$ and varying forcing amplitudes are shown in figure 9. These solutions are generated using a relaxation scheme (MATLAB's BVP4C, using the default error tolerances) and begin from a trial based on the final state computed in the initial-value problem; the solution can be then extended to different parameter settings using continuation. Also displayed

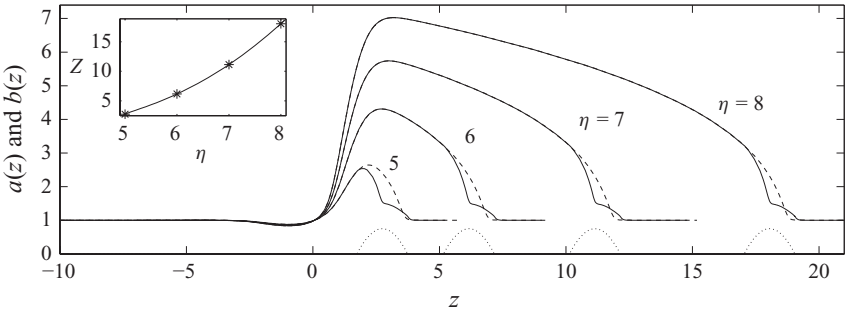

FIGURE 9. Steady particle-entraining wave solutions to (5.2)–(5.3) with $\ell = 2$, $B = 3/4$ and four values of η. The solid lines show $a(z)$ and the dotted lines show $b(z)$. The dashed lines show the solitary wave profiles with no entrained object. The inset shows the object position versus η with the four cases displayed marked by stars; $D = 1$, as in all our computations.

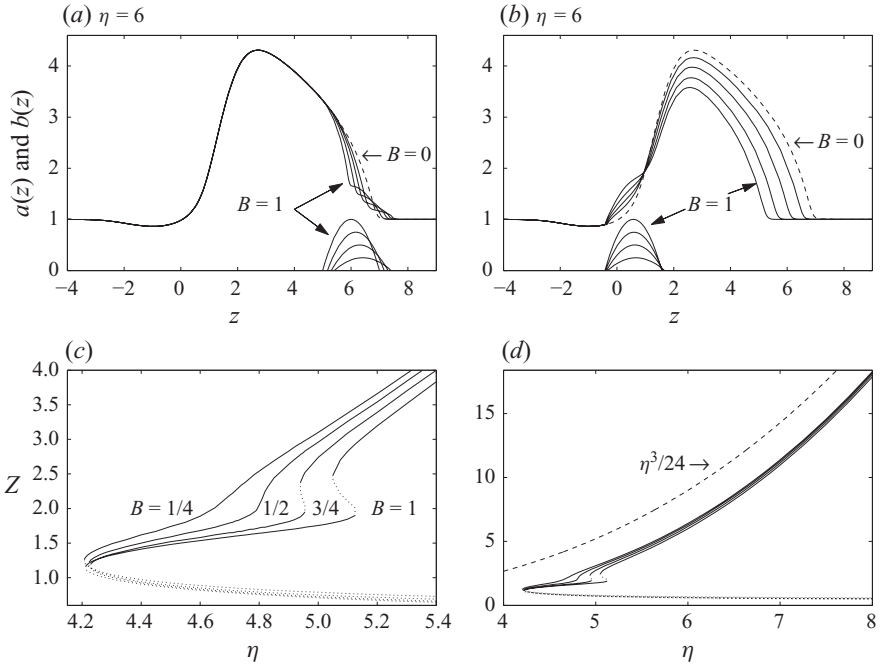

FIGURE 10. Particle-entraining wave profiles and particle positions for $\ell = 2$, $B = 1/4$, $1/2$, $3/4$ and 1. (a) The stable solutions with larger Z; (b) the unstable solutions with closer particle positions. The dashed line shows the pure-fluid solitary wave ($B = 0$). (c, d) Z versus η, with unstable branches plotted by dotted lines. In (d), the dashed line shows $\eta^3/24$.

in the figure are the solitary wave profiles predicted when there is no entrained object (i.e. $B = 0$; see Part 1). As for the pure-fluid solitary waves, when the forcing amplitude increases, a bow wave builds up ahead of the forcing. The associated pressure gradient drives the object further upstream, limiting its effect on the deformation of the tube. Consequently, the profile of $a(z)$ resembles the pure-fluid solitary wave everywhere except at the leading edge of the bow wave.

More solutions to the eigenvalue problem with varying B are shown in figure 10. The solutions can be continued to higher forcing amplitude without difficulty.

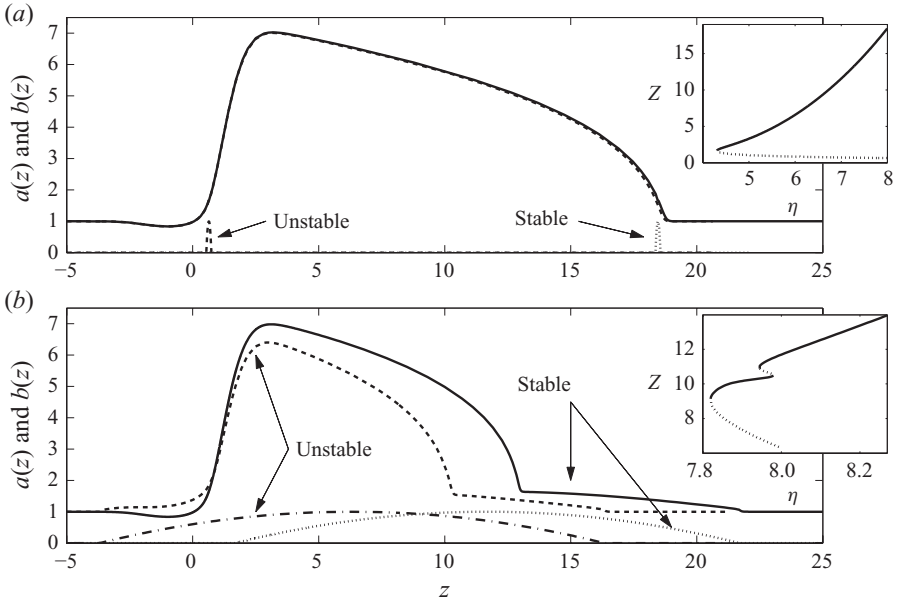

FIGURE 11. Steady solutions for (*a*) $\ell = 0.2$ and (*b*) $\ell = 20$. In each case, the stable (solid and dotted) and unstable (dashed and dot-dashed) solutions for $\eta = 8$ and $B = 1$ are shown. The insets show the object position against η.

However, the solution branches develop richer structure as η is reduced: for bigger object radii, B, the solution branches turn around to produce non-monotonic curves of Z against η, reflecting a more complicated interaction between the object and the forcing. In addition, all the branches eventually end at sufficiently small forcing amplitude by intersecting other branches of solutions that exist for smaller Z, as illustrated in figure 10(*b*). These other steady states turn out to be unstable solutions of the partial differential system (2.10)–(2.13), which can be verified by using them to begin initial-value calculations. Thus, the failure of the solitary wave to capture the object found earlier for the initial-value problem can be interpreted alternatively as the disappearance of steady particle-entraining solutions. This equivalence is not perfect: the initial-value problem with $\eta = 4.36$ in figure 7 does not capture the particle despite the existence of a steady solution at this forcing amplitude (see figure 10*c*). Thus, not all initial conditions for the partial differential system access that state when the forcing amplitude is close to its threshold, opening up a gap between the two interpretations. Loosely speaking, in the initial-value computation, if the particle penetrates through the solitary wave barrier to a position beyond the unstable equilibrium, it is not captured.

Note that, because the object is pushed out to the leading edge of the bow wave for the stable solutions at high forcing amplitude, the position Z can be estimated using the results of Part 1, where we have shown that the large-amplitude solitary waves have bow waves that extend a distance $\eta^3/24$ ahead of the forcing. Thus, $Z \sim \eta^3/24$ for $\eta \gg 1$, as indicated by figure 10(*d*).

The objects in the examples presented in figures 9 and 10 have lengths similar to the forcing region. Waves entraining much shorter and longer objects are illustrated in figure 11. The shorter object barely affects the peristaltic solitary wave and is driven along almost passively (the arguments in § 5.4 indicate that the object must therefore

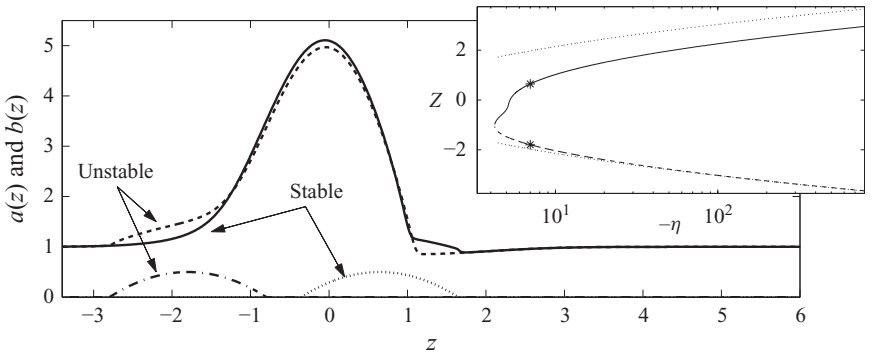

FIGURE 12. Steady solutions for waves of expansion. The main panel shows a and b for a stable–unstable pair of particle-entraining waves with $\eta = 7$, $B = 1/2$ and $\ell = 2$ (the stable solution is shown by the solid and dotted lines and the unstable solution is shown by dashed and dash-dotted lines). The inset shows the object position against $-\eta$, along with the (dashed) curves $\pm\sqrt{2\log|\eta|}$; the stable (unstable) branch is shown by the solid (dotted) lines and the stars mark the solutions shown in the main panel.

sit close to the points where $a^2 = 2$), whereas the other object is longer than the bow wave for this forcing amplitude and significantly alters its structure.

5.3. *Solitary waves of expansion*

All the preceding examples correspond to peristaltic waves of contraction: with $\eta > 0$, the forcing acts to constrict the tube. In Part 1, we have also considered waves of expansion, with $\eta < 0$, showing that transport is also possible with an outwardly directed force. Here, too, we can drive the object with a wave of expansion; an example is given in figure 12. Again, there is a pair of possible solutions for the position of the object, one stable and the other unstable, with a merger at smaller forcing amplitude occurring to generate a threshold below which the particle cannot be entrained. For an object of length $\ell = 2$ and maximum radius $B = 1/2$, the threshold (based on the disappearance of the steady solutions) is $\eta_c \approx 4.3$, and is comparable with the corresponding threshold for the waves of contraction, suggesting little difference in the ability of both waves to capture the lozenge.

As described in Part 1, the pure-fluid solitary waves of expansion develop a main peak given by $a \sim |\eta| f(z)$ for $|\eta| \gg 1$. This structure is retained for large-amplitude particle-entraining waves, with the particles in the stable–unstable pair of solutions sitting to either side of that peak (see figure 12). Given the form of our forcing in (4.4), this leads to large-$|\eta|$ estimates of the particle positions of $\pm\sqrt{2\log|\eta|}$ (see the inset of the figure). Note that the stable particle position only sits upstream of the centre of the forcing when $|\eta|$ is sufficiently large; otherwise, the particle sits downstream along with the unstable equilibrium.

5.4. *The critical threshold*

A key feature of the solutions is the critical threshold, $\eta = \eta_c$, at which the stable branch terminates, and corresponds to the smallest possible forcing amplitude required for the solitary wave to entrain the object. This threshold is plotted against the object length in figure 13 for the relatively small object radii, $B = 10^{-2}$ and $B = 1/5$. As $\ell \to 0$, the threshold converges to a constant close to 3.84. For $D = 1$, this forcing amplitude is the value at which a recirculation cell appears in the fluid underneath the solitary wave without any driven particle (Part 1). The result is relevant here

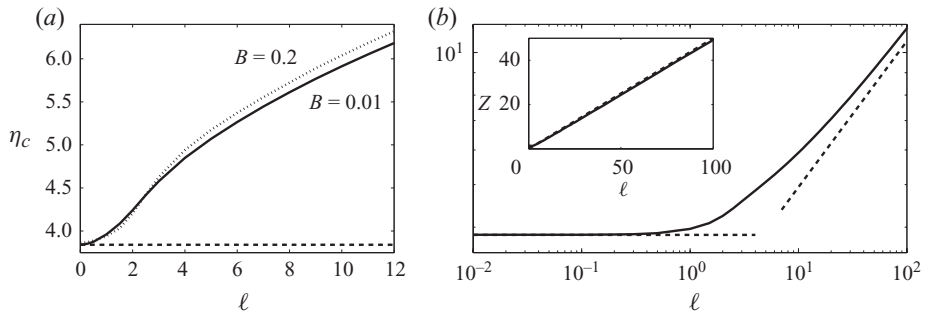

FIGURE 13. The critical forcing amplitude against ℓ for (*a*) $B = 0.01$ and $B = 0.2$, and (*b*) $B = 0.01$ over a wider range of ℓ. The horizontal dashed line shows $\eta \approx 3.84$. In (*b*), the other dashed line shows $\ell = \eta^3/12$ and the inset shows the object position at threshold together with $\ell/2$ (dashed line).

because, in the limit $B \to 0$, $1/\log(a/b) \sim 1/\log(1/B)$, $(a^2 - b^2)\,\mathrm{d}p/\mathrm{d}z \sim 8(1 - a^2)/a^2$, and the constraint (5.3) reduces to

$$\int_{Z-\ell/2}^{Z+\ell/2} \frac{(2 - a^2)}{a^2}\,\mathrm{d}z = 0, \tag{5.4}$$

where $a(z)$ is the profile of the pure-fluid solitary wave. In order to satisfy this constraint, a must exceed $\sqrt{2}$ somewhere, which is the same condition for a recirculation cell to appear. Moreover, when η is slightly above this value, and $a > \sqrt{2}$ over a narrow region, it is possible to satisfy (5.4) for sufficiently short objects by suitably adjusting Z. In other words, for short ($\ell \ll 1$), narrow ($B \ll 1$) objects, one expects particle-entraining waves for $\eta > 3.84$. This result is not unexpected: short, narrow objects act much like passive tracers, and when the pure-fluid solitary wave drives a recirculation cell, stagnation points appear in the wave frame, which may capture such tracers and provide the equilibrium particle positions.

In contrast, when the object is longer, one cannot balance the region where $a > \sqrt{2}$ against the adjoining areas with $a < \sqrt{2}$ unless the solitary wave amplitude is larger and the former regions are correspondingly longer. Thus, the threshold η_c must increase with ℓ, as seen in figure 13. The construction that furnishes the particle position which satisfies the $B \to 0$ constraint in (5.4) is illustrated in figure 14: by sliding windows of fixed length ℓ around a zero-crossing of $(2 - a^2)/a^2$, one can find a location for which positive and negative areas under the curve exactly cancel, thus satisfying (5.4). In fact, it is clear from the structure of $(2 - a^2)/a^2$ drawn in this picture that there are two possible particle positions that satisfy the constraint; these positions correspond to the two eigenvalues of the stable–unstable solution branches described above.

Note that when the object is very short ($\ell \ll 1$) but not necessarily thin (B is order one), the preceding argument does not apply because we must use the full form of the constraint (5.3). Nevertheless, as seen in figure 11(*a*), the solution for $a(z)$ is not significantly affected by the object when $\ell \ll 1$ even when B is order one. Consequently, the constraint reduces to (5.4) everywhere but close to the object, which must therefore position itself near the points where $a^2 = 2$, as in the example shown in figure 11(*a*).

The driving 'density' illustrated in figure 14 also offers an explanation for the stability of the two different steady solutions: as indicated by a suitable reduction

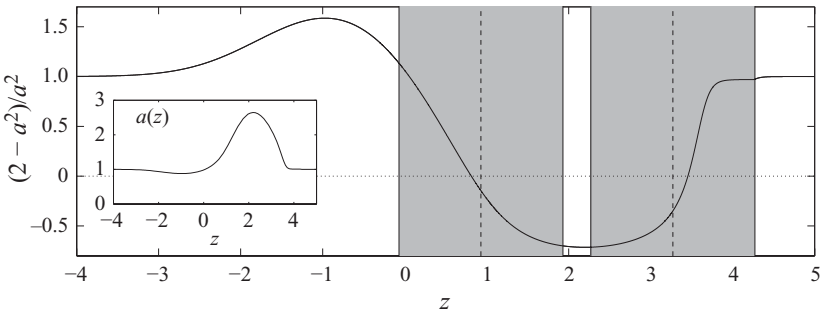

FIGURE 14. The quantity $(2-a^2)/a^2$ for a pure-fluid solitary wave with $\eta = 5$ (the inset shows $a(z)$). The shaded regions show the sections of width 2 that integrate to zero and therefore fulfil the constraint (5.4).

of (2.13), the net driving force on the object is given by the integral of $-(2-a^2)/a^2$ over the length of the object, or, equivalently, minus the area underneath the curve within one of the shaded areas in figure 14. Thus, for the particle located at the front of the bow wave, if a perturbation is introduced that pushes the particle ahead of the equilibrium position, the net driving force *decreases* (when the right-hand shaded window is shifted to the right in figure 14, the area under the curve increases). The particle therefore falls behind in the wave frame, returning to its equilibrium position. Conversely, if the particle is allowed to fall slightly behind the equilibrium position (sliding the right-hand window to the left in the figure), the driving force *increases*, again pushing the particle back towards to its stable position. For the other steady solution, exactly the opposite situation prevails, and any disturbance leads to an unstable progression of the particle away from the equilibrium.

For relatively large object lengths and small radii, figure 13 also illustrates how $\eta \to (12D^2\ell)^{1/3}$ and $Z \to \ell/2$ at threshold. In other words, the object position, Z, and half-length, $\ell/2$, limit to the length of the bow wave, $\eta^3/24D^2$ (see also the large ℓ solutions in figure 11*b*). This is consistent with the constraint in (5.4), since the tube radius in the bow wave satisfies $(Da^3/12)' + 1 \sim (2-a^2)/a^2$, with $a^3 \sim \eta^3/D^3 - 24z/D$ (implying the integral in (5.4) is equivalent to $\ell - \eta^3/12D^2$ for $\eta \gg 1$ and $Z \sim \ell/2$). Thus, as the object becomes longer, the forcing amplitude must correspondingly increase in order to provide the driving force needed to push the object along.

6. Driving finite objects with a periodic wavetrain

6.1. *Initial-value computations*

Finally, we consider how a periodic wavetrain drives finite-length objects. To accomplish the task, we again resort to time-stepping the initial-value problem (2.10)–(2.13), but now make the problem periodic in z with $f(z) = \sin z$, and place a single object in the domain with a shape given by (5.1). In other words, we consider peristaltic wavetrains passing over a periodic array of parabolic-shaped lozenges. Provided the spacing between those objects is sufficiently large, we anticipate that in between the interactions with the lozenges, the waves relax to steady structures much like the profiles built in Part 1, and so the driving of each lozenge is largely independent of the others. Nevertheless, this periodic problem is not equivalent to driving an isolated object with an infinite train of periodic waves: the object modifies passing waves, and the disfigured waves are then reinjected back into the periodic

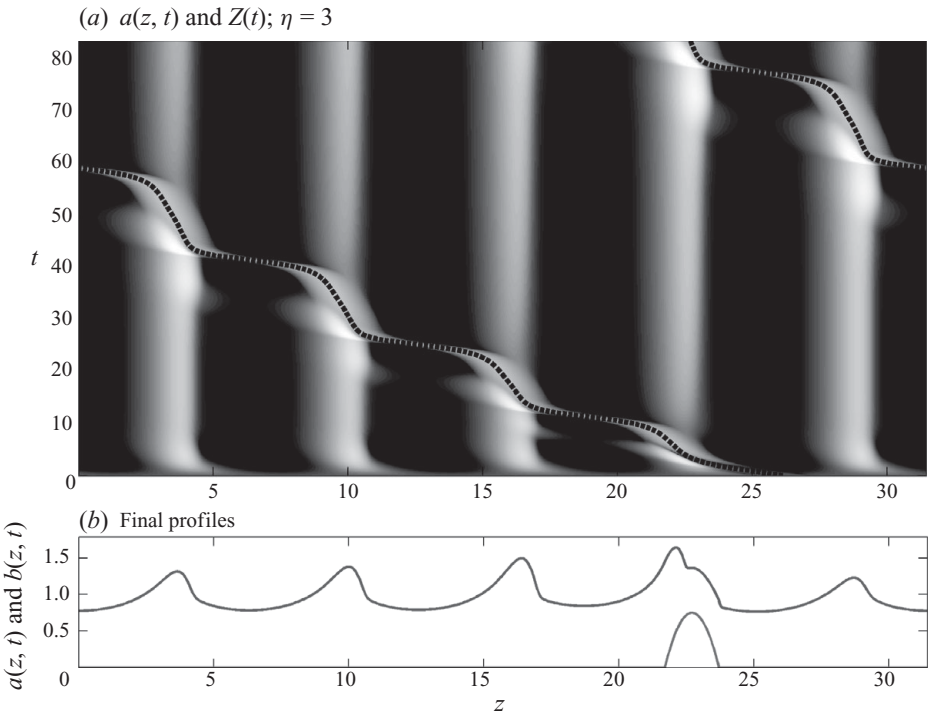

FIGURE 15. Initial-value problem with $\eta = 3$, $\ell = 2$ and $B = 3/4$ in a periodic domain of length 10π. (*a*) The tube radius as a density on the (z, t)-plane, with the dotted line showing the position of the centre of the object. (*b*) The final profiles of $a(z, t)$ and $b(z, t)$. A comparison of (*a*) and (*b*) provides a guide to the shading scheme used in (*a*).

domain upstream so that the subsequent wave–particle interactions are not with fresh waves. As a result, the dynamics becomes complex, and we opt for a relatively brief discussion to keep the exercise manageable.

We take a domain length of 10π (so that there are five peristaltic waves in the domain), initialize with $Z(0) = 50\pi/6$ and $a(z, 0) = 1$, and evolve the system until $t = 500$ or the solution has converged to an asymptotic state. Two sample solutions for a lozenge of length $\ell = 2$ (with differing forcing amplitudes) are shown in figures 15 and 16. In the first example in figure 15, the forcing strength is not sufficient for any of the waves to capture the lozenge, which consequently proceeds backwards in the wave frame, progressing stutteringly through a sequence of interactions with the waves. The higher amplitude example in figure 16, on the other hand, is entrained by the first wave it encounters. As shown by the final snapshot from the computation, the steady train that results contains a series of unequal waves, with the lozenge suppressing the amplitude of the wave that captured it, and the following waves picking up the additional fluid shed during the interaction. Note that the final state from the initial-value computation has not yet converged to the steadily propagating solution, which is also shown in figure 16(*b*). The latter solution is constructed explicitly using methods similar to those employed for solitary waves in § 5.2. The main difference is that, to construct the solution, we are no longer able to use the far-field conditions to fix $Q = -1$ in (2.11). Instead, we retain that quantity as an additional eigenvalue and determine its value by imposing the constraint (3.3).

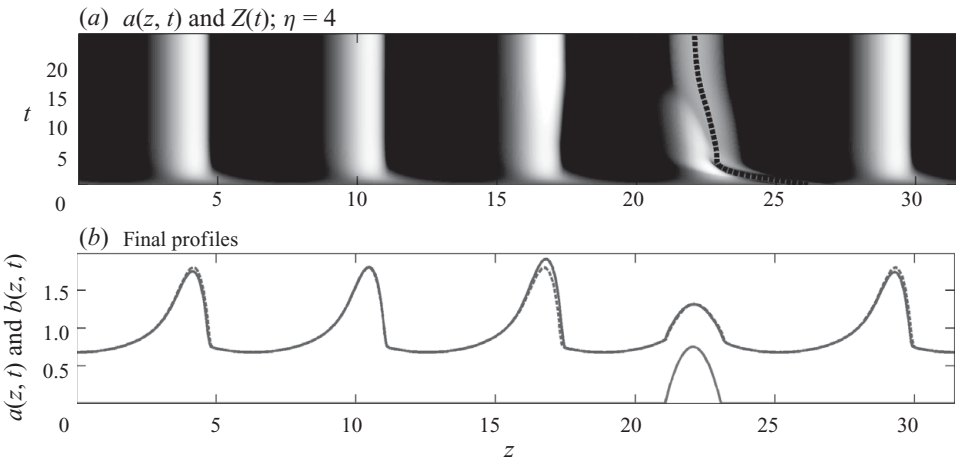

FIGURE 16. Initial-value problem with $\eta = 4$, $\ell = 2$ and $B = 3/4$ in a periodic domain of length 10π. (*a*) The tube radius as a density on the (z, t)-plane, with the dotted line showing the position of the centre of the object. (*b*) The final profiles of $a(z, t)$ and $b(z, t)$. The dashed line shows a direct computation of the steadily propagating, particle-entrained wave profile. A comparison of (*a*) and (*b*) provides a guide to the shading scheme used in (*a*).

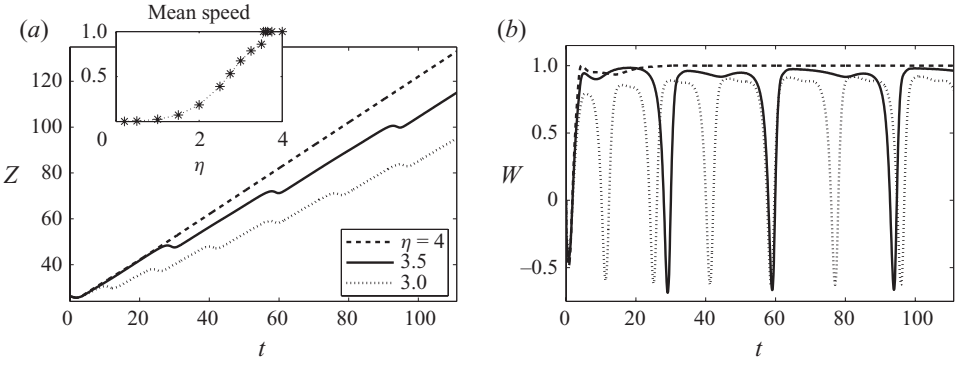

FIGURE 17. (*a*) Position and (*b*) speed for $\eta = 3$, 3.5 and 4, with $\ell = 2$ and $B = 3/4$. The inset in (*a*) shows the average speeds for a suite of computations with varying η.

As with the solitary waves, there is, therefore, a threshold forcing amplitude above which the wavetrain captures the object. Unlike the solitary-wave case, however, below threshold, the object is not simply left behind, but moves at an average speed greater than zero and less than unity due to the repeated interactions with the wavetrain, see figure 17. These unsteady, sub-threshold states correspond to temporally periodic solutions whose period lengthens as one approaches the threshold from below (in the manner of a homoclinic bifurcation); simultaneously, the average object speed increases up to unity.

For the two examples of figures 15 and 16, the lozenge has a length similar to each peristaltic wave. A temporally periodic solution for a longer object is shown in figure 18. This figure shows snapshots of the tube and lozenge profiles as the object travels from one wave to the next, and also plots estimates of the average object speed against ℓ for fixed forcing amplitude. The average object speed decreases as the

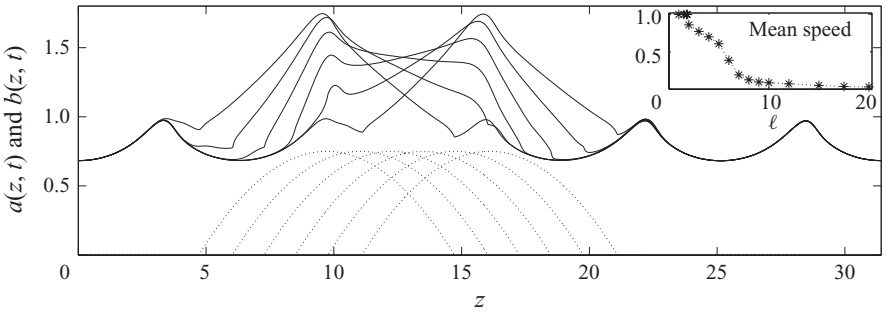

FIGURE 18. Snapshots of $a(z,t)$ and $b(z,t)$ for $\ell = 10$, $\eta = 3.5$ and $B = 3/4$. Six equally spaced snapshots are shown during the progression of the particle from one wave to the next. The inset shows the mean speed against ℓ for the same values of η and B.

object length increases, much as found earlier for the net sub-threshold displacement induced by solitary waves.

In the specific example shown in the figure (with $\ell = 10$ and $\eta = 3$), the wavetrain is barely able to push the lozenge forward and its mean speed is less than 0.1. Indeed, the object now dams up a significant fraction of the fluid, leading to a localized bulge in the tube that travels along with the object (so the computation is quite different from the interaction of an isolated lozenge with an infinite wavetrain). The object can be driven faster by raising the forcing amplitude; for $\eta = 10$, the mean speed is increased above about 0.3. However, the inability of the wavetrain to drive the object forward is pronounced when ℓ is large, and the computations become increasingly prone to error if one continues to raise η (primarily because of the development of finely scaled, steep blisters). As a consequence, we have not pushed the computations to sufficiently high forcing amplitude to determine whether there is still a critical value of η above which the wavetrain captures long lozenges or if entrainment becomes unattainable. We argue that the latter situation is most likely because, when the object length increases, at some stage it completely fills the domain. Any further increase in the parameter ℓ allows the periodic array of lozenges to overlap, forming an infinitely long corrugated rod. As $\ell \to \infty$, the corrugations become ironed out, leaving the uniform rod of § 3 which travels at a constant speed slower than that of the waves.

6.2. *The limit* $B \ll 1$

To shed more light on the dynamics of long lozenges, we take the limit $B \ll 1$, which affords further analytical headway. In this limit, the lozenge becomes too slender to affect the peristaltic waves and is driven along passively (provided the tube does not become excessively constricted). Thus, ignoring any initial transients required to establish the periodic wavetrain, the equation of motion of the object becomes (on multiplying (2.13) by $\log(1/B)$ and then taking the limit $B \to 0$)

$$W = -\frac{1}{4\ell}\int_{Z_w-\ell/2}^{Z_w+\ell/2} a^2 \frac{\partial p}{\partial z}\,\mathrm{d}z \equiv -\frac{2}{\ell}\int_{Z_w-\ell/2}^{Z_w+\ell/2} (1-q-a^2)\,\frac{\mathrm{d}z}{a^2}, \tag{6.1}$$

where $Z_w = Z - t$ is the particle position in the wave frame, $a(z)$ is the solution for the steady periodic wavetrain, explored in detail in Part 1, and $q = 1 + Q$ is the associated fluid transport constant.

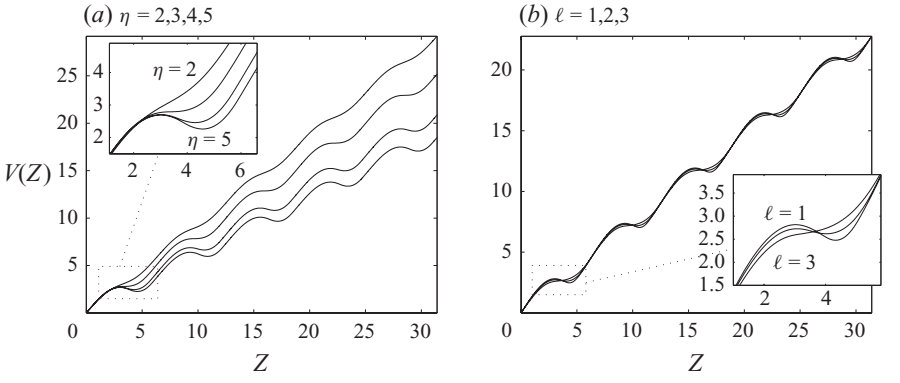

FIGURE 19. Potentials $V(Z)$ for (*a*) $\ell = 2$ and varying η (as indicated), and (*b*) $\eta = 3.5$ and varying ℓ (as indicated).

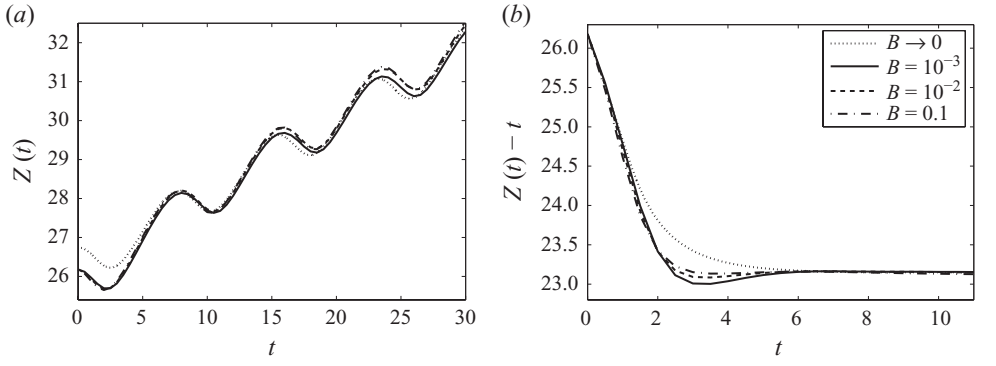

FIGURE 20. A comparison of computations of the object position $Z(t)$ for varying object radii (as indicated), with the case $B \to 0$ corresponding to the asymptotic theory. In (*a*), $\eta = 2$. In (*b*) $\eta = 4$ and the position is shown in the wave frame (i.e. we plot $Z(t) - t$).

Equation (6.1) may be rewritten as an equation for an overdamped oscillator,

$$\frac{\mathrm{d}Z_w}{\mathrm{d}t} + \frac{\mathrm{d}}{\mathrm{d}Z_w} V(Z_w) = 0, \qquad V(Z_w) = \frac{2}{\ell} \int \int_{Z_w - \ell/2}^{Z_w + \ell/2} (1 - q - a^2) \frac{\mathrm{d}z}{a^2} \, \mathrm{d}Z_w. \tag{6.2}$$

Sample potentials are shown in figure 19 for various values of forcing strength and object length. These 'washboard'-like potentials contain a periodic array of local minima when the object length is either sufficiently small or the forcing amplitude is sufficiently large. These minima correspond to stable equilibrium positions for the object and disappear at a threshold $\eta = \eta_c$, depending on the object length, where they merge with the unstable equilibrium positions. Above threshold, the particle slides left in the wave frame with periodic oscillations due to the remaining bumps in $V(Z_w)$. These features of the asymptotic solution mirror the numerical results outlined earlier (and are similar to the onset of stick–slip motion of a drop driven across an inhomogeneous surface, as explored by Thiele & Knobloch 2006).

Detailed comparisons between the asymptotic $B \ll 1$ theory and numerical computations are provided in figure 20. This figure shows computations with different lozenge radii B for two forcing amplitudes, one below and one above the threshold. Because the initial-value computations begin from an undeformed tube, but the $B \ll 1$

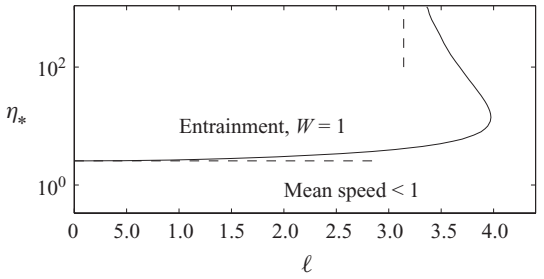

FIGURE 21. The critical amplitude $\eta = \eta_*$ for which the potential loses its minima, plotted on the (ℓ, η)-plane. The dashed lines show the limits $\eta_* \to 2.557$ for $\ell \to 0$ and $\ell \to \pi$ for $\eta_* \to \infty$.

asymptotics use the steady wave profile, the computations and asymptotics cannot agree at early times; however, both converge to similar solutions after a transient. For the sub-threshold case in figure 20(a), the initial position $Z(0)$ has been adjusted in the $B \ll 1$ theory, so that the curves can be better compared after the transient. An alternative would be to use the steady wave profile as the initial condition of the computation.

The variations in $V(Z_w)$ with η and ℓ suggest that it might be possible to continually raise the forcing amplitude to counter the flattening of the potential incurred on increasing ℓ (figure 19), thereby allowing the entrainment of arbitrarily long objects. This possibility can be discounted, however, by observing that when $\ell \to 2\pi$ in (6.2), the potential becomes linear in Z_w because the integral in z is then exactly over the period of the wavetrain and does not then depend on Z_w. Thus, all equilibria must disappear as the object length approaches the wave spacing.

To examine in more detail when entrainment fails for $B \ll 1$, we calculate the critical amplitudes $\eta = \eta_*$, for which the potential loses its minima. The results are displayed on the (ℓ, η)-plane in figure 21 and indicate that entrainment fails when the object length reaches about $\ell = 4$. As also shown in figure 21, the critical amplitude has the limit $\eta_* \to 2.557$ for $\ell \to 0$, which corresponds to the creation of recirculation cells underneath the pure-fluid periodic wavetrain along with the associated stagnation points that trap passive tracers. In addition, $\eta_* \to \infty$ for $\ell \to \pi$, which can be established using the $\eta \gg 1$ asymptotic solutions of Part 1: in this limit, the periodic wavetrains develop narrow blisters separated by severe occlusions of the tube (cf. § 3.3). The integral over z in the potential $V(Z)$ is then dominated by the occluded region where $a \sim O(\eta^{-1/2})$, and can be evaluated analytically, with the key results that $V(Z_w)$ becomes independent of η and loses its minima for $\ell = \pi$.

In other words, entrainment fails because the forces that drive the object forward cannot be arbitrarily increased by raising the forcing amplitude, but reach a limit. Note that this result applies strictly when $1 \ll \eta \ll B^{-1/2}$; for $\eta = O(B^{-1/2})$, the solution for the occluded region is of the order of the lozenge radius, and it is no longer justified to set $b \to 0$. That is, when the forcing is raised too much, the tube tightens around the lozenge within the occluded regions, and the object no longer behaves passively.

7. Conclusion

In this article, we have presented an elastohydrodynamic lubrication theory for the peristaltic pumping of rigid objects down a fluid-filled tube. By imposing a force on the tube wall, we self-consistently solved for the elastic deformation of the tube, the internal fluid flow and the motion of the enclosed object. We have considered two

types of solid objects, an infinitely long rod with constant radius and a parabolic lozenge of finite length. We drove both with either a periodic wavetrain or a peristaltic wave with solitary form.

For the infinite rod, peristaltic waves develop profiles much like their counterparts without the rod, and we have offered analytical results for low and high forcing strength, bridging the gap in between with numerical solutions. Although a solitary wave is never able to provide enough traction to move the rod, periodic wavetrains can propel it at a finite speed that is always less than the wave speed. Because heightened viscous dissipation in occlusions of the tube impedes progress if the rod is forced too strongly, the speed of propulsion achieves a maximum at a moderate forcing amplitude.

Finite lozenges can be propelled by solitary waves and we have established that there is a threshold forcing amplitude above which the waves are sufficiently strong to entrain the object and push it along at the wave speed. Below the threshold, the object cannot keep up with the peristaltic waves and falls behind, suffering only a finite displacement. The threshold increases strongly with the axial length of the object, indicating that the length of the object is an important physical parameter.

Lozenges that are shorter than the spacing of waves in a periodic train can also be entrained and driven at the wave speed beyond a critical forcing amplitude. Below that threshold, the lozenge moves stutteringly forward as a result of repeated interactions with the waves in the train, creating time-periodic states with a lower mean speed. Entrainment appears to become unattainable once the lozenge becomes too long, with very slender objects failing to be entrained once their length exceeds just over half of the wave spacing.

An important limitation of our model is that we incorporate a relatively simple, linear elastic model for the tube resistance. In Part 1, we have explored how variations in this model, whilst remaining in the framework of linear elasticity, might change the dynamics. For periodic peristaltic waves, the variations do not suggest that a qualitatively different picture would emerge when the wavetrain drives a rigid object. For solitary waves, however, the picture must necessarily change because we observed that a stiffness with higher-order axial derivatives can terminate the isolated solitary wave solution branch at finite forcing amplitude, the consequence of which remains to be explored. Moreover, nonlinear elastic effects could well play an equally key role. A better approach in this situation may be to attack the governing fluid equations numerically in conjunction with an empirical tube model based on real physiology, a task that, although more computationally intensive and less analytically accessible, is at least free of some of the approximations.

This research began at the 2009 Geophysical Fluid Dynamics Summer Program, Woods Hole Oceanographic Institution, which is supported by the National Science Foundation and the Office of Naval Research. We thank the participants for discussions, especially W. R. Young and J. B. Keller.

REFERENCES

Bertuzzi, A., Salinari, S., Mancinelli, R. & Pescatori, M. 1983 Peristaltic transport of a solid bolus. *J. Biomech.* **16** (7), 459–464.

Carew, E. O. & Pedley, T. J. 1997 An active membrane model for peristaltic pumping. Part 1. Periodic activation waves in an infinite tube. *J. Biomech. Engng* **119**, 66–76.

Connington, K., Kang, Q., Viswanathan, H., Abdel-Fattah, A. & Chen, S. 2009 Peristaltic particle transport using the lattice Boltzmann method. *Phys. Fluids* **21**, 053301.

Cummings, L. J., Waters, S. L., Wattis, J. A. D. & Graham, S. J. 2004 The effect of ureteric stents on urine flow: reflux. *J. Math. Biol.* **49** (1), 56–82.

Eytan, O. & Elad, D. 1999 Analysis of intra-uterine fluid motion induced by uterine contractions. *Bull. Math. Biol.* **61**, 221–238.

Fauci, L. J. 1992 Peristaltic pumping of solid particles. *Comput. Fluids* **21**, 583–598.

Fauci, L. J. & Dillon, R. 2006 Biofluidmechanics of reproduction. *Annu. Rev. Fluid Mech.* **38**, 371–394.

Fitz-Gerald, J. M. 1969 Mechanics of red-cell motion through very narrow capillaries. *Proc. R. Soc. Lond.* B **174** (1035), 193–227.

Fung, Y. C. 1971 Peristaltic pumping: a bioengineering model. In *Urodynamics: Hydrodynamics of the Ureter and Renal Pelvis* (ed. S. Boyarsky, C. W. Gottschalk, E. A. Tanagho & P. D. Zimskind), pp. 178–198. Academic.

Hung, T. K. & Brown, T. D. 1976 Solid-particle motion in two-dimensional peristaltic flows. *J. Fluid Mech.* **73**, 77–96.

Jiménez-Lozano, J., Sen, M. & Dunn, P. F. 2009 Particle motion in unsteady two-dimensional peristaltic flow with application to the ureter. *Phys. Rev.* E **79** (4), 41901.

Lighthill, M. J. 1968 Pressure-forcing of tightly fitting pellets along fluid-filled elastic tubes. *J. Fluid Mech.* **34** (1), 113–143.

Shapiro, A. H., Jaffrin, M. Y. & Weinberg, S. L. 1969 Peristaltic pumping with long wavelengths at low Reynolds number. *J. Fluid Mech.* **37** (4), 799–825.

Siggers, J. H., Waters, S., Wattis, J. & Cummings, L. 2008 Flow dynamics in a stented ureter. *Math. Med. Biol.* **26**, 1–24.

Srivastava, L. M. & Srivastava, V. P. 1989 Peristaltic transport of a particle-fluid suspension. *J. Biomech. Engng* **111**, 157–165.

Skotheim, J. & Mahadevan, L. 2005 Soft lubrication: the elastohydrodynamics of conforming and non-conforming contacts. *Phys. Fluids*, **17**, 092101.

Takagi, D. & Balmforth, N. J. 2011 Peristaltic pumping of viscous fluid in an elastic tube. *J. Fluid Mech.* **672**, 196–218.

Thiele, U. & Knobloch, E. 2006 Driven drops on heterogeneous surfaces: onset of sliding motion. *Phys. Rev. Lett.* **97**, 204501.